SIMULATION AND ANALYSIS OF A NOVAL THERMAL MANAGEMENT SYSTEM INTEGRATED WITH HEAT PIPE RADIATORS FOR 4680 BATTERY MODULE

Yang LIU[1], Jian-ming LI[2], Qing MA[2], Ya-xiong WANG[2,3,4]*

[*1]School of Chemistry & Chemical Engineering, Inner Mongolia University of Science & Technology, Baotou 014010, China

[2]School of Mechanical Engineering, Inner Mongolia University of Science & Technology, Baotou 014010, China

[3]Inner Mongolia Key Laboratory of Coal Chemical Engineering & Comprehensive Utilization, Baotou 014010, China

[4]Inner Mongolia BriTech Co., Ltd., Baotou 014030, China

[*]Corresponding author; E-mail: 149416922@qq.com

In order to enhance the safety and service life of automotive 4680 cylindrical batteries during high current discharge state, based on theoretical analysis and numerical simulation, a novel air cooling thermal management system that is integrated with finned heat pipe radiators has been developed and studied in this paper. A triangular heat conduction area was developed by leveraging the gaps within an equilateral triangular arrangement of cylindrical batteries to enhancement heat transfer and improve energy density, and heat exchange between finned heat pipes and cold air is facilitated by varying numbers of fins. Simulation results indicates that with the ambient temperature of 298.15K and wind speed of 13m/s, the maximum temperature of the battery module is 310.81K and the temperature difference is 4.59K under a 4C discharge rate. In additional, the temperature difference within the battery module reduces by 4.78% through optimizing the airflow duct and structure parameters of fins, which offering insights and references for the optimization and application of thermal management of automotive battery modules in the future.

Key words：*Battery thermal management; Air cooling; Heat pipe radiators; Numerical simulation; Temperature Uniformity*

1. Introduction

The transportation industry has always been considered a major source of global greenhouse gas emissions. In recent years, people have become increasingly concerned about environmental issues, and electric vehicles have been widely introduced and used to address the energy consumption and environmental damage caused by traditional fuel-powered cars [1]. Currently, electric vehicles can mainly be divided into three categories: Battery Electric Vehicles (BEVs), Hybrid Electric Vehicles (HEVs) and Fuel Cell Vehicles (FCVs). BEVs rely entirely on electric power for propulsion, thus offering advantages such as zero tailpipe emissions, ease of operation and quick response time,

making them an ideal alternative to traditional fuel-powered vehicles. For BEVs, the battery module is the core power component, and batteries with larger capacity and lower self-discharge can ensure longer travel distances for electric vehicles.

Lithium-ion batteries, as the power source for electric vehicles, have significant potential. Currently, based on differences in technological approaches and application scenarios among manufacturers, there are three development directions for lithium-ion batteries: cylindrical batteries, prismatic batteries, and pouch batteries. Among these, the cylindrical batteries offer many advantages such as higher energy density per unit volume, no memory effect, long cycle life and more mature technological pathways [2,3], making them widely adopted by various companies in their respective products, such as Tesla's Model S, Model X, and Model Y. The Model Y, in particular, utilizes Tesla's proprietary tabless 4680 battery, which, compared to the 18650 and 21700 batteries, has higher energy density and power output [4], making it an excellent choice for electric vehicles.

However, lithium-ion batteries also have some significant issues that cannot be ignored. The efficiency of lithium-ion batteries is highly affected by temperature [5], and excessive working temperatures can impact the stability and capacity of the batteries [6], even trigger thermal runaway [7]. Additionally, fast charging generates additional heat [8]. Therefore, during the operation of electric vehicles, it is necessary to control the temperature of the battery module within a suitable range. Large temperature differences can also affect the rate of battery degradation, consistency, and the performance of charging and discharging, ultimately impacting the overall lifespan of the battery module. Based on extensive previous research, lithium-ion batteries demonstrate optimal performance within the temperature range of 298 K to 313 K, and the temperature difference within the battery module should be controlled within 5 K [9]. In order to mitigate the adverse effects of temperature variations on battery performance, thermal management measures need to be implemented to control and manage the battery module temperature [10]. Currently, the primary method for battery thermal management is through external temperature control. This paper mainly focuses on about the strengthening of heat dissipation of battery thermal management.

Currently, there are two types of cooling methods for automotive battery modules: active cooling and passive cooling. Active cooling includes methods such as air cooling and liquid cooling, while passive cooling includes methods like thermoelectric cooling and heat pipe cooling [11]. In active cooling, air cooling primarily removes the heat generated by the battery by flowing air over its surface [12]. Currently, research on air cooling primarily focuses on factors such as airflow arrangement, contact angle between air and battery surface, airflow velocity, and air temperature. Compared to other cooling methods, air cooling has advantages such as a simple heat dissipation structure, low cost, and ease of maintenance, making it the most mature cooling method currently. The application of heat pipes in Battery Thermal Management Systems (BTMS) is one of the current research highlights. Rao et al. [13] and Behi et al. [14] conducted cooling effect tests by directly attaching flat heat pipes to the battery surface, and the results showed that heat pipes effectively control battery temperature. Liu et al. [15] enhanced the performance of heat pipes by adding fins to the condensation section. Zhang et al. [16] inserted flat heat pipes between two batteries to achieve cooling of the batteries. Numerical studies have demonstrated the potential of using nanofluids to enhance the thermal performance of thermosiphons in electronic cooling applications by J Jose et al. [17].

When utilizing automotive battery modules, the limited space results in a decrease in the effective heat dissipation area between batteries.Given that high-rate charging and discharging of the batteries generate considerable heat, passive cooling alone does not adequately reduce the battery surface temperature. Therefore, active cooling methods must be incorporated. However, the traditional liquid cooling methods entail intricate channel networks throughout the battery module, which introduce safety risks such as liquid leakage and add to system complexity, thereby affecting its stability. Therefore, the current research is of great significance from the perspective of reducing the battery spacing and improving the overall energy density and safety of the battery module. This study explores the peak temperature and temperature difference inside the densely packed cylindrical battery module, and solves the thermal management problem of the cylindrical battery through air cooling and heat dissipation by heat pipes cooling, fundamentally avoiding the leakage risk caused by the liquid cooling solution.

2. Thermal model

The thermal model is used to describe the temperature distribution inside the battery module, which is usually divided into two aspects: heat generation and heat transfer. As the 4680 batteries is a wound cylindrical battery, the heat generation of the battery starts from the inside of the battery cell and gradually conducts to the outside over time. This process follows Fourier's law, and therefore the temperature distribution of the battery can be represented by the following formula.

$$\rho C_p \frac{\partial T}{\partial t} = \frac{\partial}{\partial x}(\lambda \frac{\partial T}{\partial x}) + \frac{\partial}{\partial y}(\lambda \frac{\partial T}{\partial y}) + \frac{\partial}{\partial z}(\lambda \frac{\partial T}{\partial z}) + q_v \tag{1}$$

2.1. Battery heat generation model

In an electrochemical reaction process of a battery, energy changes inevitably occur, known as reaction heat. These changes manifest as either the absorption or release of heat. When the battery discharges, there is a negative enthalpy change, resulting in the external environment receiving energy. On the other hand, when the battery charges（CC-CV）, a positive enthalpy change takes place, causing heat to be absorbed from the external environment.

Additionally, there is Ohmic heat produced due to the internal resistance of the battery. This resistance generates heat as the current passes through, following Joule's law where the amount of heat generated is directly proportional to the square of the current.

Furthermore, polarization heat is observed during the charging and discharging process of the battery. This occurs due to shifts in the electrode potential, resulting in polarization phenomena and the release of a certain amount of heat.

Moreover, side reaction heat occurs when the battery is subjected to abnormal states such as high temperature, overcharging, or over-discharging during the charging and discharging process. This heat, accompanying side reactions, is usually minimal and can be disregarded in engineering applications, except in extreme situations. [17]

Therefore, the heat generated during the regular operation of a lithium-ion battery can be represented by equation (2).

$$Q_{battery} = Q_r + Q_o + Q_p + Q_s \tag{2}$$

Where, $Q_{battery}$ is the total amount of heat generated by the battery. Q_r is the heat generated during the electrochemical reaction. Q_o is the Ohmic heat, commonly known as Joule heat, caused by the internal resistance of the battery. Q_p is the heat generated due to polarization phenomena that occur during the charging and discharging processes. Q_s is the heat generated as a result of side reactions.

Due to experimental constraints, it is not possible to investigate the heat generation mechanism of the 4680 battery through experiments. Therefore, it is advisable to refer to previous research on heat generation in batteries. Currently, the most widely used model for battery heat generation is the aggregate model[19].

$$q=\frac{I}{V}[(E-U)+T\frac{dU}{dT}] \tag{3}$$

Where, q is the heat generation rate per unit volume of the battery, W/m^3; I is the current, A; V is for the volume of the battery, m^3; E is the electromotive force of the battery, V; U symbolizes the terminal voltage, V; T is the temperature, K; dU/dT is the temperature coefficient or entropy coefficient, mV/K.

In the Bernardia model, $I\ (E-U)$ represents the irreversible reaction heat in the heat source, while $ITdU/dT$ represents the reversible reaction heat in the heat source. According to the research of Bernardia et al., when assuming the battery to be a uniform internal heat source and the heat generation in the battery mainly comes from internal resistance and entropy increase reaction, the calculation of battery heat generation can neglect reaction heat and polarization heat.

2.1.1 Irreversible reaction heat

The irreversible heat in the Bernardia equation can be expressed as follows:

$$Q_{ir}=I^2(r_o+r_p) \tag{4}$$

Where, Q_{ir} is the power of irreversible heat, W ; r_o is the ohmic resistance, Ω; r_p is the polarization resistance, Ω.

Therefore, the Bernardia equation can be reformulated as follows:

$$q=\frac{I}{V}[I(r_o+r_p)+T\frac{dU}{dT}] \tag{5}$$

2.1.2 Reversible reaction heat

By breaking down the Bernardia equation, the expression for reversible reaction heat can be obtained as follows:

$$Q_{re}=IT\frac{dU}{dT} \tag{6}$$

Where, Q_{re} is the reversible reaction heat, W. In reference to existing literature, the Automobile Engineering Research Institute of Jiangsu University conducted experimental tests on the entropy heat coefficient of ternary lithium batteries [20]. The obtained entropy heat coefficients were fitted, resulting in the determination of the average entropy heat coefficient of ternary lithium batteries under various State of Charge (SOC) conditions, which is demonstrated below:

$$0.5<SOC\leq 1:\frac{dU}{dT}=0.66\cdot SOC^2-1.48\cdot SOC+0.67 \quad (7)$$

$$0.2<SOC\leq 0.5:\frac{dU}{dT}=3.33\cdot SOC^3-3.50\cdot SOC^2+1.32\cdot SOC-0.10 \quad (8)$$

$$0\leq SOC\leq 0.2:\frac{dU}{dT}=2.00\cdot SOC^2-0.20\cdot SOC-0.07 \quad (9)$$

The reversible reaction heat of the 4680 battery can be calculated using the variable entropy heat coefficient at different discharge rates and SOC.

2.2. Battery heat generation rate of 4680 cell

The battery's heat generation rate model under different SOC states can be obtained by organizing the above-mentioned formulas for reversible and irreversible reaction heat calculations：

$$0.5<SOC\leq 1:q=\frac{I}{V}[IR_{re}+T(0.66\cdot SOC^2-1.48\cdot SOC+0.67)] \quad (10)$$

$$0.2<SOC\leq 0.5:q=\frac{I}{V}[IR_{re}+T(3.33\cdot SOC^3-3.50\cdot SOC^2+1.32\cdot SOC-0.10)] \quad (11)$$

$$0\leq SOC\leq 0.2:q=\frac{I}{V}[IR_{re}+T(2.00\cdot SOC^2-0.20\cdot SOC-0.07)] \quad (12)$$

The study employed 4680 ternary lithium-ion batteries measuring 46mm in diameter and 80mm in height. These batteries have a rated voltage of 3.5V and a capacity of 26Ah. The positive electrode consists of high-nickel ternary material $Li[Ni_{1-x-y}Co_xMn_y]O_2$ (NCM), while graphite serves as the negative electrode, and the electrolyte is lithium hexafluorophosphate. Heat generation power of the battery under various states of charge (SOC) and discharge rates at an ambient temperature of 298.15K can be determined through the calculation mentioned above, with the outcomes depicted in Fig. 1.

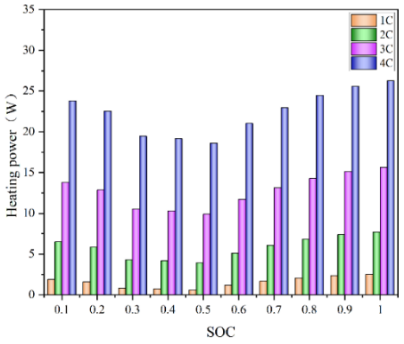

Figure 1. Thermal power generation of battery cell under different SOC and C-rate

2.3. Thermal resistance of heat pipes

Due to the use of a regular triangular staggered arrangement, the internal layout of the module is compact, requiring the use of heat pipes to transfer internal heat to the cooling end. To simplify the numerical calculations, the heat pipe is considered as an equivalent heat conductor possessing an

exceptionally high thermal conductivity. Consequently, it becomes essential to compute the equivalent thermal conductivity and thermal resistance of the heat pipe. As the heat transfer in the heat pipe mainly occurs axially and the vapor chamber has an extremely high thermal conductivity, the total thermal resistance of the heat pipe, R_{hp}, is mainly composed of the thermal resistance of the wall surface and the liquid absorption core. The calculation formula is as follows:

$$R_{hp}=R_{eva,w}+R_{eva,wk}+R_{con,w}+R_{con,wk} \tag{13}$$

$$R_{eva,w}=\frac{ln(r_{hp}/r_{wk})}{2\pi\lambda_w l_{eva}} \tag{14}$$

$$R_{eva,wk}=\frac{ln(r_{wk}/r_{st})}{2\pi\lambda_{wk} l_{eva}} \tag{15}$$

$$R_{con,w}=\frac{ln(r_{hp}/r_{wk})}{2\pi\lambda_w l_{con}} \tag{16}$$

$$R_{con,wk}=\frac{ln(r_{wk}/r_{st})}{2\pi\lambda_{wk} l_{con}} \tag{17}$$

Equations (13)-(17) provide the calculation formulas for the thermal resistance of each component. In these equations, R_{hp} is the total thermal resistance of the heat pipe, K/W; $R_{eva,w}$ is the radial thermal resistance of the evaporation section wall, K/W; $R_{eva,wk}$ is the radial thermal resistance of the evaporation section wick, K/W; $R_{con,w}$ is the radial thermal resistance of the condensation section wall, K/W; Similarly, $R_{con,wk}$ is for the radial thermal resistance of the condensation section wick, K/W; r_{hp} is the outer radius of the heat pipe, m; r_{wk} is the outer radius of the wick, m; and r_{st} is the inner radius of the heat pipe, m. Additionally, λ_w is the heat conductivity of the heat pipe wall, $Wm^{-1}K^{-1}$, while λ_{wk} is the heat conductivity of the wick, $Wm^{-1}K^{-1}$. Furthermore, l_{eva} is the length of the evaporation section of the heat pipe, m; and l_{con} is the length of the condensation section of the heat pipe, m.

For the convenience of theoretical calculation and simulation, this paper equates the thermal superconducting properties of the heat pipe to a heat conduction tube with extremely high thermal conductivity. The calculation of the equivalent thermal conductivity of the heat pipe is carried out using Equation 18 [21]. Since the heat transfer mechanism in the heat pipe primarily depends on the phase change of the internal working fluid, the calculation of thermal resistance focuses solely on the radial component. The expression for the equivalent thermal conductivity λ_{eff} of the heat pipe is defined as follows:

$$\lambda_{eff}=\frac{4l_{hp}}{R_{hp}\pi d^2} \tag{18}$$

where, λ_{eff} is the equivalent thermal conductivity of the heat pipe, $Wm^{-1}K^{-1}$; l_{hp} is the length of the heat pipe, m; d is the outer diameter of the heat pipe, m.

3. Numerical simulation

The software ANSYS Fluent is used to investigate and optimize the heat dissipation performance of the battery thermal management module, The calculation process follows the continuity equation, momentum equation, and energy equation [22].

$$\frac{\partial \rho}{\partial t}+\frac{\partial \rho u}{\partial x}+\frac{\partial \rho v}{\partial y}+\frac{\partial \rho w}{\partial z}=0 \tag{19}$$

$$\begin{aligned}
\rho\left(\frac{\partial u}{\partial t}+u\frac{\partial u}{\partial x}+v\frac{\partial u}{\partial y}+w\frac{\partial u}{\partial z}\right)&=\rho f_x-\frac{\partial p}{\partial x}+\mu\left(\frac{\partial^2 u}{\partial x^2}+\frac{\partial^2 u}{\partial y^2}+\frac{\partial^2 u}{\partial z^2}\right)\\
\rho\left(\frac{\partial v}{\partial t}+u\frac{\partial v}{\partial x}+v\frac{\partial v}{\partial y}+w\frac{\partial v}{\partial z}\right)&=\rho f_y-\frac{\partial p}{\partial y}+\mu\left(\frac{\partial^2 v}{\partial x^2}+\frac{\partial^2 v}{\partial y^2}+\frac{\partial^2 v}{\partial z^2}\right)\\
\rho\left(\frac{\partial w}{\partial t}+u\frac{\partial w}{\partial x}+v\frac{\partial w}{\partial y}+w\frac{\partial w}{\partial z}\right)&=\rho f_z-\frac{\partial p}{\partial z}+\mu\left(\frac{\partial^2 w}{\partial x^2}+\frac{\partial^2 w}{\partial y^2}+\frac{\partial^2 w}{\partial z^2}\right)
\end{aligned} \tag{20}$$

$$\frac{\partial}{\partial t}(\rho_w c_{pw} T_w)+\nabla\cdot(\rho_w c_{pw}\vec{v}T_w)=\nabla\cdot(k_w\nabla T_w) \tag{21}$$

The *k*-*ε* RNG model is used to accurately calculate the momentum variations of fluid during heat dissipation and the Coupled scheme is adopted, the flow Reynolds number set to 200 during the simulation process.

The RNG turbulent kinetic energy transport equation[23]:

$$\frac{\partial}{\partial t}(\rho k)+\frac{\partial}{\partial x_i}(\rho k u_i)=\frac{\partial}{\partial x_i}\left(\alpha_k \mu_{eff}\frac{\partial k}{\partial x_j}\right)+G_k+G_b-\rho\varepsilon-Y_M+S_k \tag{22}$$

RNG model turbulent dissipation rate transport equation[23]:

$$\frac{\partial}{\partial t}(\rho\varepsilon)+\frac{\partial}{\partial x_i}(\rho\varepsilon u_i)=\frac{\partial}{\partial x_i}\left(\alpha_\varepsilon \mu_{eff}\frac{\partial \varepsilon}{\partial x_j}\right)+C_{1\varepsilon}\frac{\varepsilon}{K}\left(G_k+C_{3\varepsilon}G_b\right)-C_{2\varepsilon}\rho\frac{\varepsilon^2}{k}-R_\varepsilon+S_\varepsilon \tag{23}$$

The discrete form of the pressure gradient term in the momentum equation in the Coupled algorithm is as follows:

$$\sum_f p_f A_k=-\sum_f a^{u_k p} p_j \tag{24}$$

The discrete form of the momentum equation is given by the following expression:

$$\sum_j a_{ij}^{u_k u_k} u_{kj}+\sum_j a_{ij}^{u_k p} p_j=b_i^{u_k} \tag{25}$$

The discrete form of the continuity equation is as follows:

$$\sum_k\sum_j a_{ij}^{p u_k} u_{kj}+\sum_j a_{ij}^{pp} p_j=b_i^p \tag{26}$$

The governing equation can be written in the following form:

$$A_{ij}=\begin{bmatrix} a_{ij}^{pp} a_{ij}^{pu} a_{ij}^{pv} a_{ij}^{pw} \\ a_{ij}^{up} a_{ij}^{uu} a_{ij}^{uv} a_{ij}^{uw} \\ a_{ij}^{vp} a_{ij}^{vu} a_{ij}^{vv} a_{ij}^{vw} \\ a_{ij}^{wp} a_{ij}^{wu} a_{ij}^{wv} a_{ij}^{ww} \end{bmatrix} \overrightarrow{X_j}=\begin{bmatrix} p_i' \\ u_i' \\ v_i' \\ w_i' \end{bmatrix} \overrightarrow{B_i}=\begin{bmatrix} -r_i^p \\ -r_i^u \\ -r_i^v \\ -r_i^w \end{bmatrix} \quad (27)$$

3.1. Boundary Conditions and Assumptions

Assumption of Conditions：

(1) The fluid is incompressible.

(2) The heat generation rate of the battery is constant and thermal conductivity is isotropic.

(3) The physical properties do not change with temperature.

(4) The ambient temperature remains constant.

(5) The contact thermal resistance is ignored.

The following are the boundary conditions of the simulation:

(1) Three batteries in the middle of the model are set to a volume generation rate of 172,994.5 W/m^3. The front and rear surfaces of the four TCAs are set as adiabatic surfaces, while the surfaces of the remaining TCAs are set as constant heat flux with a density of 1989.43 W/m^2. The top and bottom ends of the batteries are set as adiabatic surfaces.

(2) The ambient temperature and initial temperature are both set at 298.15K.

3.2. Battery simulation and modeling

The temperature behavior of battery cell under natural convection conditions was modeled and investigated. In order to maintain consistency with subsequent experiments, the heat source with a diameter of 15mm and a length of 70mm was placed inside the cylindrical model. Both the heat source and the shell material were made of aluminum, and the wall boundary condition was set to a convective heat transfer coefficient of h = 16 Wm^{-2}K^{-1} on the battery surface. The obtained the predicted temperature versus time curve (Figure 2) for the battery cell under natural convection conditions at different discharge rates.

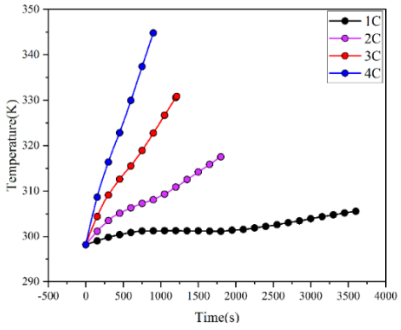

Figure 2. Temperature of battery cells under different C-rates

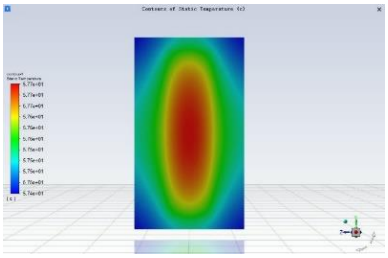

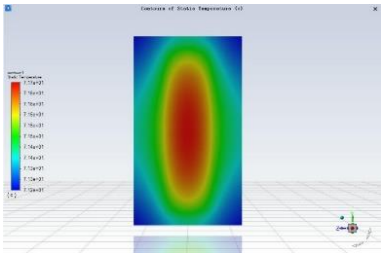

Figure 3: Temperature contour map of battery under natural convection at 3C-rate

Figure 4: Temperature contour map of battery under natural convection at 4C-rate

C-rate refers to the current value needed to charge/discharge the rated capacity of a battery within a specified time period, numerically equivalent to multiples of the battery's rated capacity. From Fig. 2, it can be observed that as the battery rate increases, the termination temperature of the battery cells rises rapidly. Under a 3C rate, the maximum surface temperature of the battery reached 330.85K at 1200 seconds, and under a 4C rate, it even reached 344.85K at 900 seconds. Based on the data, it can be concluded that without effective heat dissipation measures, the safety and stability of the battery will be greatly affected. Fig. 3 and Fig. 4 display the temperature distribution of the heat generated by the battery under high discharge rates.

3.3. Thermal management system design

Fig. 5, 6 and 7 show the schematic diagram of the thermal management system. The thermal management system consists of the battery cells and finned heat pipes. The battery module consists of seventeen 4680 cells arranged in a regular triangle, and the spacing between any two cells is 2mm, as shown in Figure 6. There is a triangle gap between any three cells due to the external structure of the 4680 battery cell is cylindrical inside the battery modules. In order to improve the space utilization rate within the modules, the triangular thermal conduction area (TCA) was designed and created a circular

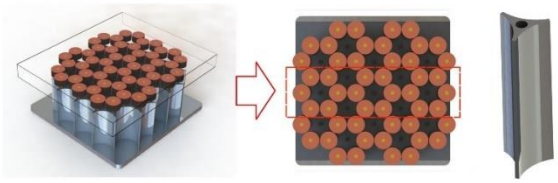

Figure 5. Schematic diagram of BTMS

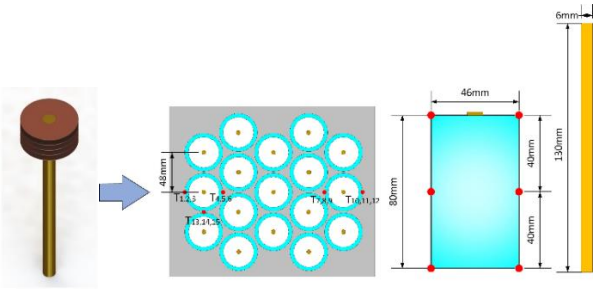

Figure 6. Thermal management model measurement point diagram and structural dimension diagram

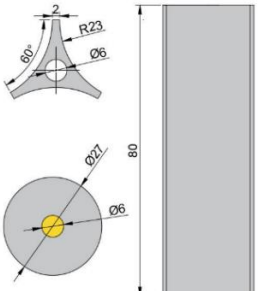

Figure 7. TCA dimensional drawing

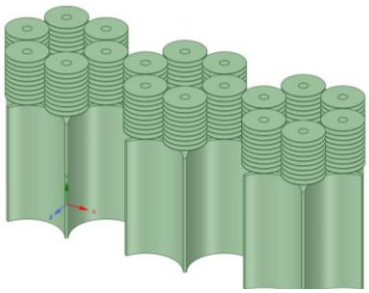

Figure 8. Simulation model structure diagram

Table 1. Physical property parameters

Name	Density (kg/m^3)	Specific heat capacity ($Jkg^{-1}K^{-1}$)	Thermal conductivity ($Wm^{-1}K^{-1}$)
Battery	2780	1000	202.4

TCA	2719	871	202.4
Heat pipe	8978	381	6768
Fins	8978	381	381

hole with an outer diameter of 6mm and a depth of 75mm in the center of TCA. In these holes, the finned heat pipes are arranged where the length of the heat pipes is 130mm, the diameter of the fins is 27mm, the spacing of the fins is 3mm, and the thickness of the fins is 0.3mm. Due to the symmetry of the battery module structure, in order to reduce the calculation load and improve the efficiency, the subsequent simulation work is carried out using the red dashed line shown in Figure 5. The overall structure of the simulation model is shown in Fig. 8. The optimal heat dissipation solution is determined by changing the number of fins on the heat pipe. The three types of finned heat pipes have 5, 10, and 15 fins respectively, and they will be referred to as Style1, Style2, and Style3 in the subsequent articles. Table 1 summarizes the material properties in the thermal management system.

3.4. Grid division and grid independence analysis

As shown in Fig. 9, the image after the model grid division, local dimensions were added to the battery and heat pipe with a grid size of 0.3 and a growth rate of 1.2. Boundary layers were added to the air duct with the boundary layer type set to smooth-transition, adding a total of 3 layers with a transition ratio of 0.272. The volume grid adopts polyhedra with a growth rate of 1.2, and the maximum element size is 3.29. The image below shows the image after the model grid is divided, with local sizes added to the batteries and heat pipes, a mesh size of 0.3, growth rate of 1.2. Boundary layers are added to the air duct, with the boundary layer type as smooth-transition. 3 layers of transition are added with a ratio of 0.272. The volume grid uses polyhedra with a growth rate of 1.2 and the maximum unit is 3.29. Under the operating condition of 4C multiplication and a wind speed of 13m/s, four different mesh numbers were selected for comparison. From Fig. 10, it can be observed that when the mesh number reaches 12,000,000, the calculation results tend to stabilize with an error within 0.4%. Therefore, the simulation will be conducted with this mesh quantity.

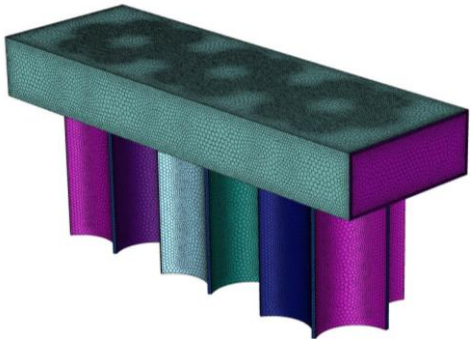

Figure 9. Mesh generation

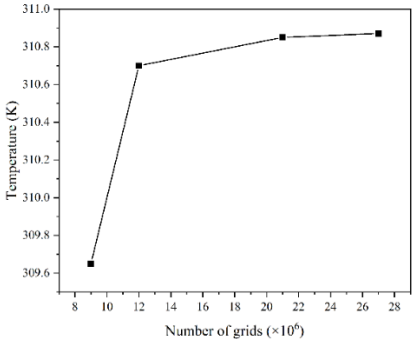

Figure 10. Mesh independence analysis

3.5. Thermal management system simulation

Fig. 11 shows the temperature variation over time under the conditions of 4C rate and a wind speed of 11m/s. It is shows that T1 is the lowest temperature, while T9 corresponds to the highest temperature. This phenomenon can be attributed to the battery module's design, which incorporates

heat dissipation structures at both ends. These structures ensure efficient heat dissipation at the front and rear, leading to comparatively lower temperatures at the outermost ends.

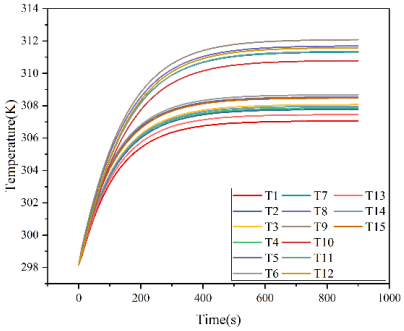

Figure 11. Temperature of various temperature measurement points at 4C C-rate and 11m/s

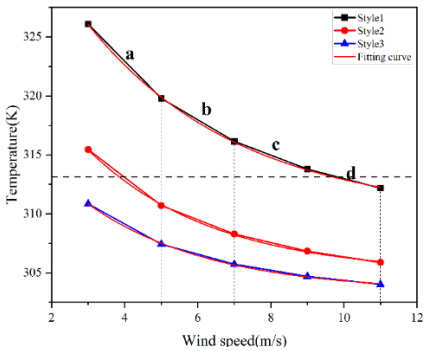

Figure 12. Maximum temperature on the surface of the battery at different airflow velocities and numbers of fins under 3C

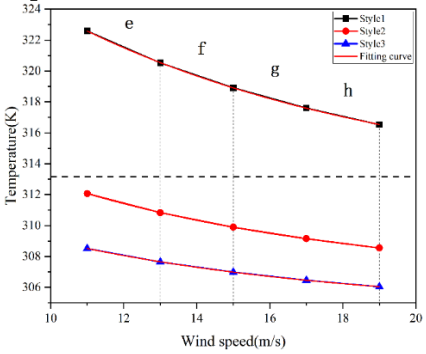

Figure 13. Maximum temperature on the surface of the battery at different airflow velocities and numbers of fins under 4C

From Fig. 12 and Fig. 13, it can be observed that:

1. Under the same multiplication rate, the same heat transfer area, and an increase in wind speed to a certain extent, the decreasing trend in temperature gradually weakens when the multiplication rate, heat transfer area, and wind speed increase to a certain extent, aligning with previous research [24]. By fitting the curves, the functional relationship can be established between the battery surface temperature and wind speed, as represented by Equation (28). The coefficients of the parameters are provided in Table 2. The results indicates that although the number of fins may differ, the trend of the maximum temperature curves under different wind speeds is consistent, which suggests that under the same load and heat transfer area, there exists an exponential relationship between wind speed and temperature.

2. Comparing Style 1, Style 2 and Style 3, it can be observed that under Style 1 conditions, the maximum temperature decreases more significantly with increasing wind speed. A analysis of this phenomenon can be made as follows: When the number of fins is small, the heat dissipation area of the module is small. The unremoved heat increases the battery temperature, resulting in a larger heat transfer temperature difference between the battery and the cold fluid in the air duct. At this time, increasing the wind speed can significantly increase the heat dissipation power. As the number of fins increases, the increase in heat dissipation area reduces the unremoved heat. This in turn reduces the heat transfer temperature difference between the battery surface and the cold fluid, leading to a decreasing impact of wind speed on heat dissipation power.

$$y=A_1 \cdot e^{\left(-\frac{x}{T_1}\right)}+Y_0 \tag{28}$$

Table 2. Fit the parameters of the formula

C-rate	Style	A_1	T_1	Y_0
3C	Style1	33.2±0.63	4.1±0.183	309.8±0.320
	Style2	25.1±0.90	3.4±0.193	304.9±0.234
	Style3	18±0.73	3.4±0.210	303.3±0.181
4C	Style1	34.6±0.57	9±0.253	312.2±0.192
	Style2	21.7±0.56	8±0.270	306.4±0.118
	Style3	15.2±0.37	8.1±0.259	304.5±0.080

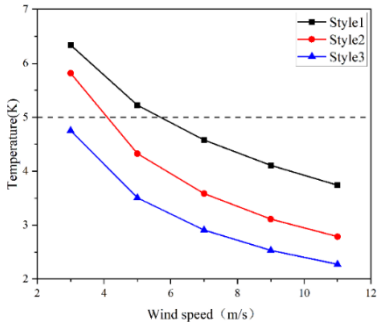

Figure 14. Temperature difference in the module under different number of fins at 3C C-rate

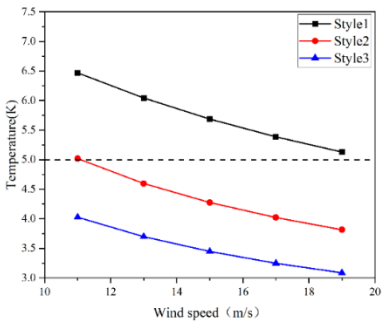

Figure 15. Temperature difference in the module under different number of fins at 4C C-rate

From Fig. 14 and Fig. 15, the following observations can be made:

1.The trend of temperature difference in the battery module is the same for all three styles with respect to changes in wind speed.

2.Comparing the curves of maximum temperature and temperature difference under the same C-rate, it can be observed that the number of fins has a greater impact on the maximum temperature compared to the temperature difference under the same wind speed conditions. According to Newton's cooling formula, maximum temperature is mainly influenced by the heat transfer area and convective heat transfer coefficient. The temperature difference inside the battery module is closely related to the structure of the cooling device. When the device structure remains unchanged, the trend of the temperature difference inside the battery module tends to stabilize.

The above analysis indicates that increasing the heat transfer area and fluid flow rate can indeed improve the heat dissipation performance. However, as the heat transfer area and flow rate increase, the benefits of heat dissipation gradually decrease. Therefore, it is necessary to find the optimal solution that maximizes the benefits within the given constraints. Since the optimal operating temperature for lithium-ion batteries is 293.15-313.15K, the maximum temperature difference on the battery surface inside the battery module should be less than 5K. The components that meet this condition at 3C and 4C rates are indicated by dashed lines in Figures 12, 13, 14, and 15. When operating at 3C rate, Style1 requires a wind speed greater than 11m/s, Style2 requires a wind speed greater than 5m/s, and Style3 requires a wind speed greater than 3m/s. When operating at 4C rate, Style2 requires a wind speed greater than 13m/s, and Style3 requires a wind speed greater than 11m/s.

Additionally, the slope of each curve section can be observed in Table 3, revealing that the temperature variation rate is higher in region b for Style2 at 3C rate and in region f for Style2 at 4C rate, while still meeting the optimal operating temperature conditions for lithium-ion batteries. The maximum temperatures in these regions are 310.7K and 310.81K, and the maximum temperature differences are 4.33K and 4.59K, respectively.

Considering the practical application perspective, since battery modules are used in electric vehicles, the height of the battery module should not be excessively high. Comparing Style 2 and Style 3, the height of the battery module is 16.5mm higher in Style3 compared to Style2. Under the same battery quantity, Style3 has a volume increase of 13.98%. Hence, selecting the Style2 configuration at 3C and 4C rates allows the battery module to maintain a maximum temperature within the optimal operating range while ensuring a temperature difference within the module of less than 5K. This satisfies the optimal usage conditions for the battery module.

Table 3 The slope of the curve at 3C and 4C magnification

C-rate	Name	a	b	c	d	C-rate	Name	e	f	g	h
	Style1	-3.15	-1.82	-1.175	-0.81		Style1	-1.03	-0.81	-0.65	-0.54
3C	Style2	-2.38	-1.205	-0.73	-0.48	4C	Style2	-0.62	-0.465	-0.375	-0.3
	Style3	-1.71	-0.85	-0.515	-0.345		Style3	-0.435	-0.325	-0.265	-0.215

Fig. 16 shows the temperature cloud map of Style 2 battery module at a 3C rate and a wind speed of 5m/s. Fig. 17 shows the temperature cloud map of Style 2 battery module at a 4C rate and a wind speed of 13m/s. From fig. 16 and 17, the following observations can be made: (1) Regardless of the 3C or 4C rate, the temperature trend of the battery module is the same. (2) It can be observed that in figure 16, the closed low-temperature fluid region at the upper end of the third fin heat pipe appears and extends until the fifth heat pipe. In fig. 17, the low-temperature fluid region also shows a closing trend at the third fin heat pipe, but it doesn't completely close until the last heat pipe. This indicates that in this design, when the wind speed is high, there is a part of the region that does not participate in heat exchange, which exists in the gap between the fins and the air duct. Therefore, when the wind speed is high, the spacing between the air duct and heat exchange fins can be appropriately reduced.

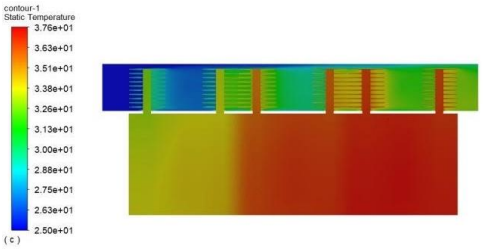

Figure 16. Temperature contour map of Style2 battery pack at 3C and 5m/s

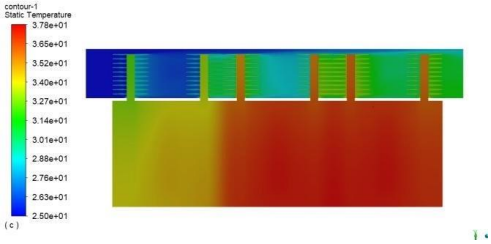

Figure 17. Temperature contour map of Style2 battery pack at 4C and 13m/s

Fig. 18 shows the relationship between the maximum temperature on the battery surface and time under 10 fins conditions at 3C and 4C rates, at wind speeds of 5m/s and 13m/s. From Fig. 18, it can be analyzed that for both operating conditions, the relationship between time and temperature follows a logarithmic function. By processing the data, it can be observed that the curve reaches a

slope of 1 at 400 seconds for the 3C rate and 300 seconds for the 4C rate. This indicates that the rate of temperature change decreases after these two time points.

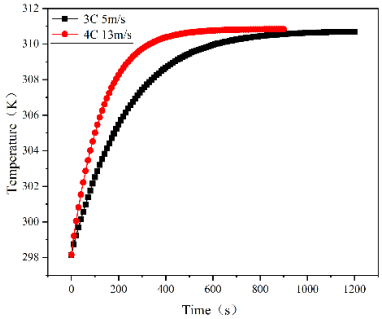

Figure 18. Maximum temperature on the surface of the battery under 3C, 5m/s and 4C, 13m/s operating

Additionally, at 300 seconds under the 4C rate, the temperature reaches 308.65K, which is 91.35% of the steady-state temperature for this condition. This suggests that the temperature rise of the battery module is very fast during the early stage under high rates. Therefore, in future research, if the addition of phase-change heat storage materials for auxiliary thermal management is considered, the phase-change temperature can be set between 298.15K and 308.65K. This can help reduce the initial temperature rise rate of the battery and, in practical applications, due to the low thermal conductivity of the battery, reducing the temperature rise rate on the battery surface can to some extent decrease the temperature difference between the inside and outside of the battery, thus potentially extending the battery's lifespan.

3.6. Installation energy accounting

The battery module must follow the law of energy conservation during operation, so the energy relationship inside the battery module follows the energy balance equation shown in Equation (29).

$$Q_{battery}=Q_f+Q_{all} \tag{29}$$

Where $Q_{battery}$ is the total heat generation of the battery during simulation, Q_f is the heat dissipation, and Q_{all} is the heat required for the temperature rise of each part inside the battery module. Taking the condition of 4C rate and a wind speed of 13m/s as an example, the average temperature difference between the inlet and outlet in the air duct is 3.79K. The average temperature rise of the battery and TCA part is 11.13K, that of the heat pipe part is 10.94K, and that of the fin part is 8.64K. According to formula (30), the required power for temperature rise in each part of the model is calculated to be 20.3W. At the same time, the total heat generation inside the model is 176.18W. Therefore, the heat dissipation power is 155.88W, and according to Newton's cooling formula, the convective heat transfer coefficient h_{f1} can be determined to be 209.95 $Wm^{-2}K^{-1}$.

$$Q=Cm\Delta T \tag{30}$$

In the equation, C represents specific heat capacity, $Jkg^{-1}K^{-1}$; m represents mass flow rate, kg/s; ΔT represents the average temperature difference between the inlet and outlet of the air duct, K. The equations (31) and (32) represent the calculation equations for the Reynolds number and convective heat transfer coefficient of the finned heat pipe respectively.[25] Through calculation, Re_f is determined to be 8092.01 and h_{f2} is calculated to be 222.38 $Wm^{-2}K^{-1}$. The calculation error between

the convective heat transfer coefficients obtained by the energy method and the formula method is 5.9%.

$$Re_f = \frac{G_{f,max} d}{\mu_f} \tag{31}$$

$$h_{f2} = 0.134 \frac{\lambda_f}{d_o} Re_f^{0.681} Pr_f^{1/3} \left(\frac{s_f}{l_f}\right)^{0.2} \left(\frac{s_f}{\delta_f}\right)^{0.1134} \tag{32}$$

4. Optimization of the thermal management scheme

4.1. Fins optimization

Fig. 19 is a line graph showing the variation of the average temperature at the outlet of the air duct with time at different wind speeds under a 4C rate. The results indicate that within the interval of 200 s to 400 s, the average temperature at the outlet tends to stabilize at all wind speeds. Meanwhile, as the wind speed increases, the average temperature at the outlet gradually decreases. Comparing the curve in the graph with equation (30), it can be observed that when all other conditions remain constant, an increase in wind speed leads to a decrease in temperature difference. This indicates that when the inlet temperature exceeds the set temperature, the desired heat dissipation power can be achieved by increasing the wind speed. When the wind speed has a smaller effect on the cooling effect of the battery module, the heat transfer efficiency of the fins can be improved by optimizing the fin thickness or changing the fin height.

$$\eta_h = \frac{Q_f}{Q_{battery}} \tag{33}$$

Where, η_h is the heat dissipation efficiency; Q_f is the heat dissipation rate, W ; $Q_{battery}$ is the heat generation rate of the battery, W.

$$\eta_h = C \cdot \frac{K_1(nr_{hp}) I_1(nr_{fin}) - I_1(nr_{hp}) K_1(nr_{fin})}{I_0(nr_{hp}) K_1(nr_{fin}) + K_0(nr_{hp}) I_1(nr_{fin})} \tag{34}$$

Where, K_0 is the modified zeroth-order Bessel function of the second kind; K_1 is the modified first-order Bessel function of the second kind; I_0 is the modified zeroth-order Bessel function of the first kind; I_1 is the modified first-order Bessel function of the first kind.

$$n = \sqrt{\frac{2h_{fin}}{\lambda_{fin}\delta}} \tag{35}$$

Where, h_{fin} is the convective heat transfer coefficient on the fin surface, measured in $Wm^{-2}K^{-1}$; λ_{fin} is the thermal conductivity of the fin, measured in $Wm^{-1}K^{-1}$; δ is the fin thickness, m.

$$C = \frac{2r_{hp}/n}{(r_{fin}^2 - r_{hp}^2)} \tag{36}$$

Where, r_{hp} is the radius of the heat pipe, m; r_{fin} is the outer diameter of the fin, m.

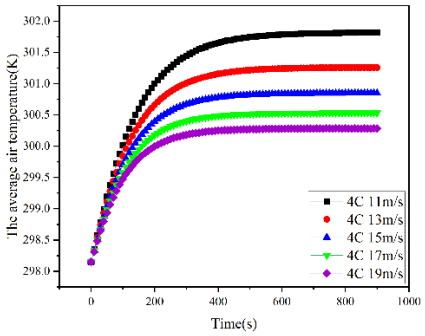

Figure 19. Average temperature at the outlet of the air duct after 900 s under 4C operating condition

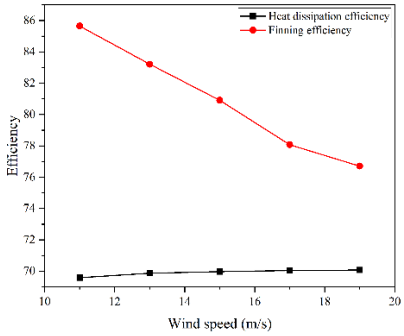

Figure 20. Heat dissipation efficiency and fin efficiency under 4C operating condition

By formula (33), the heat dissipation efficiency η_h for the 4C rate scheme can be calculated. Through formulas (34)-(36) [26], the fin efficiency η_f of this scheme can be calculated. As shown in Fig. 20, the two curves represent the heat dissipation efficiency and fin efficiency. Analyzing this graph reveals that as the wind speed increases, the cooling efficiency of the scheme does not change significantly, but the fin efficiency decreases markedly. The fin efficiency calculation formula is related to the fin thickness and height, indicating that under high wind speed conditions, fins with larger thickness and smaller height can be selected to increase the fin efficiency.

4.2. Air duct optimization

Fig. 21 is a trajectory graph of a rectangular air duct at 11m/s wind speed under the 4C rate. The parameters inside the graph show the wind speed under working conditions. It can be observed that there is an acceleration of wind speed on both sides of the air duct, and the region of accelerated flow gradually increases along the direction of fluid flow. The maximum wind speed in the region near the edge of the air duct and the fin edge reaches 20m/s. However, upon inspecting the model, it can be found that only a small portion of the accelerated region passes over the fins. In other words, the fluid in the acceleration region is not well utilized for heat exchange. Therefore, certain improvements should be made to the flow channel structure to involve the fluid in the accelerated region in heat transfer.

Fig. 22 is a trajectory graph of a variable cross-section air duct at 11m/s wind speed under the 4C rate. From the graph, it can be observed that the majority of the trajectory colors through the surface of the fins change from green to yellow. This indicates a significant increase in the flow velocity through the fins in the variable cross-section air duct. Additionally, the area of the high-speed region near the edge of the air duct, which passes over the fins, also shows some increase.

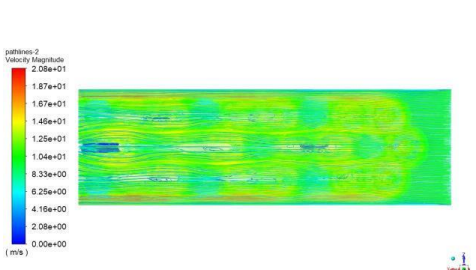

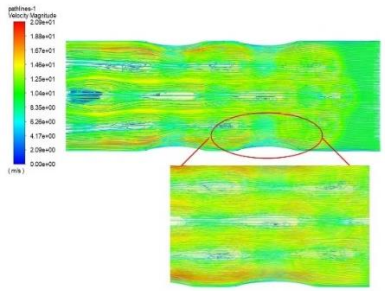

Figure 21. Velocity trace map of rectangular air duct under 4C, 11m/s operating condition

Figure 22. Velocity trace map of variable cross-section air duct under 4C, 11m/s condition

Fig. 23 and Fig. 24 show the variation of the maximum temperature and temperature difference over time for a conventional air duct and a variable cross-section air duct under the 4C rate.

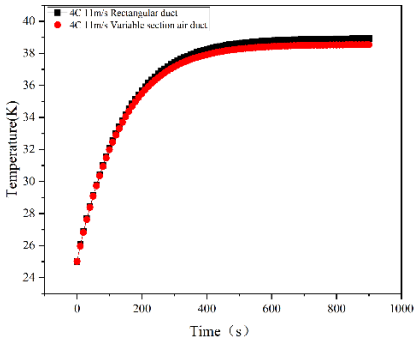

Figure 23. Maximum temperature on the cell surface in rectangular duct under 4C condition

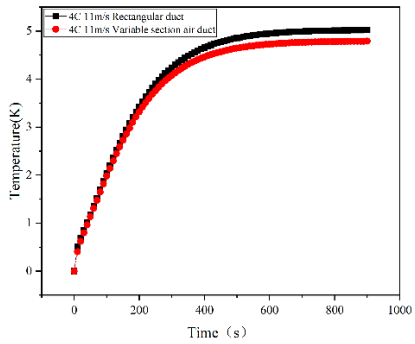

Figure 24. Maximum temperature on the cell surface in variable section duct under 4C condition

The results indicate that under the rectangular air duct, the maximum temperature on the battery surface is 312.08K with a temperature difference of 5.02K. Under the variable cross-section air duct, the maximum temperature on the battery surface is 311.68K with a temperature difference of 4.78K. It can be seen that the variable cross-section air duct doesn't significantly reduce the maximum temperature, but it reduces the temperature difference by 4.78%. As a result, the proposed scheme fulfills the requirement of maintaining a maximum total temperature difference of less than 5K for the battery module. Consequently, enhancing the design of the air duct proves beneficial in achieving a more uniform temperature distribution across the battery module. Subsequent experiments will verify this scheme and determine the optimal solution through theoretical calculations.

5. Conclusion

By utilizing the gaps generated by arranging large 4680 cylindrical batteries in an equilateral triangle pattern, a thermal management module was designed incorporating finned heat pipes and air cooling. The maximum temperature and temperature difference of the 4680 battery module under 3C and 4C rates after implementing this thermal management module were analyzed using transient numerical simulations.

The focus of the study was on exploring thermal management solutions for cylindrical batteries in densely packed configurations and high-rate charge/discharge condition, providing technical support for the application of cylindrical batteries from a heat transfer perspective.

(1) Under the condition of 4C ratio and 13m/s wind speed, the maximum temperature of the battery module can be maintained at 310.81K, and the temperature difference can be maintained at 4.59K.

(2) By using a variable cross-section airflow duct, the temperature difference of the battery module under the 4C rate, 10 fins, and 11m/s working conditions was reduced by 4.78%. Such a design helps enhance the thermal uniformity of the battery module.

device.Future research and experiments will corroborate these findings and employ theoretical calculations to ascertain the optimal diameter and thickness of the fins.

Nomenclature

C – Specific heat capacity, [kJkg^{-1}K^{-1}]
d – Diameter, [m]
E – Electromotive force, [V]
h – Convective heat transfer coefficient, [Wm^{-2}K^{-1}]
I – Electric current, [A]
I_0 – Modified zero-order Bessel function of the first kind
I_1 – Modified first-order Bessel function of the first kind
K_0 – The second kind of zero-order modified Bessel function
K_1 – The second kind of first-order modified Bessel function
l – Length, [m]
m – Mass, [kg]
Q – Heat flux, [W]
q – The heat generation rate of the battery, [W/m^3]
R – Thermal resistance, [K/W]
R' – Resistance, [Ω]
Re – Reynolds number (=UD/n)
r – Radius, [m]
T – Temperature, [K]
ΔT – Temperature difference, [K]
U – Terminal voltage, [V]
V – Volume, [m^3]

Abbreviations

BEVs – Battery Electric Vehicles
BTMS – Battery Thermal Management Systems
CC-CV – Constant-Current and Constant Voltage
FCVs – Fuel Cell Vehicles
HEVs – Hybrid Electric Vehicles
SOC – State of Charge
TCA – Triangular heat conduction area

Greek symbols

δ– Thickness, [m]
η– Efficiency
λ– Thermal conductivity, [Wm^{-1}K^{-1}]

Subscripts

all – battery module
battery – Battery
con – Heat pipe condenser section
eva – Heat pipe evaporation section
eff – Equivalent calculation
f – Fluid
fin – Fins
hp – Heat pipe
ir – Irreversible reaction
o – Ohm
p – Polarization
r – Chemical reaction
re – Reversible reaction
s – Side reaction
st – heat pipe steam chamber
w – Wall
wk – Heat pipe wick

References

[1] Raijmakers, L. H. J., *et al.*, A review on various temperature-indication methods for Li-ion batteries, *Applied Energy, 240* (2019), pp. 918-945.

[2] Wang, Q., *et al.*, A critical review of thermal management models and solutions of lithium-ion batteries for the development of pure electric vehicles, *Renewable and Sustainable Energy Reviews, 64* (2016), pp. 106-128.

[3] Liu, H. Q., *et al.*, Thermal issues about Li-ion batteries and recent progress in battery thermal management systems: A review, *Energy conversion and management, 150* (2017), pp. 304-330.

[4] Tranter, T. G., *et al.*, Communication—prediction of thermal issues for larger format 4680 cylindrical cells and their mitigation with enhanced current collection, *Journal of The Electrochemical Society, 167* (2020), 16, 160544.

[5] Lopez, C. F., *et al.*, Experimental analysis of thermal runaway and propagation in lithium-ion battery modules, *Journal of the Electrochemical Society, 162* (2015), 9, pp. A1905.

[6] Ramadass, P., *et al.*, Capacity fade of Sony 18650 cells cycled at elevated temperatures: Part I. Cycling performance, *Journal of Power Sources, 112* (2002), 2, pp. 606-613.

[7] Wang, Q., *et al.*, A review of lithium ion battery failure mechanisms and fire prevention strategies, *Progress in Energy and Combustion Science, 73* (2019), pp. 95-131.

[8] Keyser, M., *et al.*, Enabling fast charging–Battery thermal considerations, *Journal of Power Sources, 367* (2017), pp. 228-236.

[9] Pesaran, A. A., Battery thermal models for hybrid vehicle simulations, *Journal of Power Sources, 110* (2002), 2, pp. 377-382.

[10] Lipu, M. H., *et al.*, Intelligent algorithms and control strategies for battery management system in electric vehicles: Progress, challenges and future outlook, *Journal of Cleaner Production, 292* (2021), pp. 126044.

[11] Al- Zareer, M., *et al.*, A review of novel thermal management systems for batteries, *International Journal of Energy Research, 42* (2018), 10, pp. 3182-3205.

[12] Chen, K., *et al.*, Structure optimization of parallel air-cooled battery thermal management system with U-type flow for cooling efficiency improvement, *Energy, 145* (2018), pp. 603-613.

[13] Rao, Z., *et al.*, Experimental investigation on thermal management of electric vehicle battery with heat pipe, *Energy Conversion and Management, 65* (2013), pp. 92-97.

[14] Behi, H., *et al.*, Heat pipe air-cooled thermal management system for lithium-ion batteries: High power applications, *Applied Thermal Engineering, 183* (2021), pp. 116240.

[15] Liu, F., *et al.*, Dynamic thermal characteristics of heat pipe via segmented thermal resistance model for electric vehicle battery cooling, *Journal of Power Sources, 321* (2016), pp. 57-70.

[16] Zhang, Z., and Wei, K., Experimental and numerical study of a passive thermal management system using flat heat pipes for lithium-ion batteries, *Applied Thermal Engineering, 166* (2020), 114660.

[17] Jose, J., Hotta, T. K., Numerical Investigation on Thermal Performance of Nanofluid-Assisted Wickless Heat Pipes for Electronic Thermal Management, *Journal of Thermal Science and Engineering Applications, 16* (2024), 4, 041009.

[18] Smolka, J., *et al.*, 3-D coupled CFD model of a periodic operation of a heating flue and coke ovens in a coke oven battery, *Fuel, 165* (2016), pp. 94-104.

[19] Li, H. H., *et al.*, The influence of entropy heat coefficient simplification on the accuracy of thermal model of libs, *Journal of Chongqing University of Technology (Natural Science), 35* (2021), 5, pp. 1-12.

[20] Yuan, Q., *et al*., Effect of coupling phase change materials and heat pipe on performance enhancement of Li‐ion battery thermal management system, *International Journal of Energy Research, 45* (2021), 4, pp. 5399-5411.

[21] Zhang, J.,*et al*., Numerical evaluation of the heat transfer performance of water-cooled system for electric vehicle drive motor based on the field synergy principle, *Thermal Science, 28* (2024), 2A, pp. 823-835.

[22] Lim, D. C.,*et al*., Comparison of different turbulence models in pipe flow of various Reynolds numbers, *Proceedings,* AIP Conference., Kuala Lumpur, Malaysia, 2018, Vol. 2035, No.1.

[23] Zhao, J., *et al*., Thermal management of cylindrical power battery module for extending the life of new energy electric vehicles, *Applied Thermal Engineering, 85* (2015), pp. 33-43.

[24] Briggs, D. E.,Yong, E. H.,Convection heat transfer and pressure drop of air flowing across triangular pitch banks of finned tubes, *Proceeding,* Chemical engineering progress symposium series, Houston, USA,1962, Vol.59, pp. 1-10.

[25] Look, D. C., 1-D fin tip boundary condition corrections, *Heat Transfer Engineering, 18* (1997), 2, pp. 46-49.

Received: 01.02.2024.
Revised: 09.04.2024.
Accepted: 12.04.2024.